Scaling Properties of Aerosol Optical Thickness Retrieved from Ground-Based Measurements

Mikhail D. Alexandrov

Department of Applied Physics and Applied Mathematics, Columbia University, and NASA Goddard Institute for Space Studies, New York, New York

Alexander Marshak

NASA Goddard Space Flight Center, Greenbelt, Maryland

Brian Cairns

Department of Applied Physics and Applied Mathematics, Columbia University, and NASA Goddard Institute for Space Studies, New York, New York

Andrew A. Lacis and Barbara E. Carlson

NASA Goddard Institute for Space Studies, New York, New York

ABSTRACT

Statistical scale-by-scale analysis, for the first time, has been applied to the aerosol optical thickness (AOT) retrieved from the Multi-Filter Rotating Shadowband Radiometer (MFRSR) network. The MFRSR data were collected in September 2000 from the dense local network operated by the U.S. Department of Energy Atmospheric Radiation Measurement program, located in Oklahoma and Kansas. These data have 20-s temporal resolution. The instrument sites form an irregular grid with the mean distance between neighboring sites about 80 km. It is found that temporal variability of AOT can be separated into two well-established scale-invariant regimes: 1) microscale (0.5–15 km), where fluctuations are governed by 3D turbulence, and 2) intermediate scale (15–100 km), characterized by a transition toward large-scale 2D turbulence. The spatial scaling of AOT was determined by the comparison of retrievals between different instrument sites (distance range 30–400 km). The authors investigate how simultaneous determination of AOT scaling in space and time can provide means to examine the validity of Taylor's frozen turbulence hypothesis. The temporal evolution of AOT scaling exponents during the month appeared to be well correlated with changes in aerosol vertical distribution, while their spatial variability reflects the concavity/convexity of the site topography. Explanations based on dynamical processes in atmospheric convective boundary layer are suggested.

1. Introduction

Atmospheric and especially tropospheric aerosols through their effect on atmospheric processes remain a significant source of uncertainty for climate modeling and prediction (Hansen et al. 2002; Kaufman et al. 1997, 2002; Houghton et al. 2001). Modern satellites equipped with high-resolution instruments like the Moderate Resolution Imaging Spectroradiometer (MODIS), Advanced Very High Resolution Radiometer (AVHRR), Polarization and Directionality of the Earth's Reflectances (POLDAR), Total Ozone Mapping Spectrometer (TOMS), and Multi-Angle Imaging Spectroradiometer (MISR) provide retrievals of aerosol properties with global coverage. Currently available satellite aerosol products allow for the analysis of aerosol variability on various spatial scales (e.g., from 1 km to global in the case of MODIS) with 1-day temporal resolution. Ground-based sun-photometric networks [e.g., the Aerosol Robotic Network (AERONET) and Multi-Filter Rotating Shadowband Radiometer (MFRSR) networks] on the other hand provide better temporal resolution (as good as 20 s for MFRSR and 15 min for AERONET), while their spatial coverage is limited to discrete locations. Both types of datasets have one dense dimension (space for satellites, time for ground networks) and one sparse dimension. Scaling analysis of both types of aerosol datasets can help to explore their information

Corresponding author address: M. Alexandrov, NASA Goddard Institute for Space Studies, 2880 Broadway, New York, NY 10025. E-mail: malexandrov@giss.nasa.gov

content and find effective validation and data fusion mechanisms. It can also reveal the dynamical basis of aerosol variability in the atmospheric system as it relates to the height-resolved turbulence structure and airmass transport.

This paper presents a first step in this direction, describing the aerosol optical thickness (AOT) datasets in the framework of scale-invariant (fractal) statistics. We will see that the particular structure of aerosol datasets suggests that the commonly used one-point Gaussian statistics can be complemented by two-point statistics that characterize correlations between measurements of AOT at different scales. In addition to the mean and the standard deviation of the AOT distribution, we will evaluate variability over a range of scales and determine the power-law scaling exponents. As far as we are aware, this is the first attempt to use scale-invariant statistics to analyze the variability of AOT. For clouds with much stronger horizontal inhomogeneity than aerosols, this approach has been successfully applied to ground-based (e.g., Cahalan and Snider 1989; Ivanova et al. 2002), airborne (e.g., Davis et al. 1996, 1999; Marshak et al. 1997), and satellite data (e.g., Lovejoy et al. 1993; Davis et al. 1997).

We base our study on the data collected in September 2000 from the dense local MFRSR network operated by the U.S. Department of Energy (DOE) Atmospheric Radiation Measurement (ARM) program, located in the southern Great Plains (SGP) in north-central Oklahoma and south-central Kansas (see the Web site at http://www.arm.gov). It consists of 21 instruments distributed across approximately 55 000 mi^2 ($3° \times 4°$) and can be considered as an intermediate type of information source between satellite and ground-based aerosol datasets. These network data allow us to study AOT variability at the microscale (0.5–10 km) and mesoscale (10–400 km).

2. SGP MFRSR dataset

a. MFRSR measurements and retrievals

The MFRSR makes precise simultaneous measurements of the direct solar beam extinction and horizontal diffuse flux, at six wavelengths (nominally 415, 500, 615, 670, 870, and 940 nm) at short intervals (20 s in our case) throughout the day [cf. Harrison et al. (1994) for a description of the operational details]. Besides water vapor at 940 nm, the other gaseous absorbers within the MFRSR channels are NO_2 (at 415, 500, and 615 nm) and O_3 (at 500, 615, and 670 nm). Aerosols and Rayleigh scattering contribute atmospheric extinction in all MFRSR channels. The single-instrument retrievals used in this study have been made using our previously reported method (Alexandrov et al. 2002b). The retrieval products include daily time series of the aerosol optical thickness in all spectral channels and at a reference wavelength of 550 nm, column mean aerosol particle
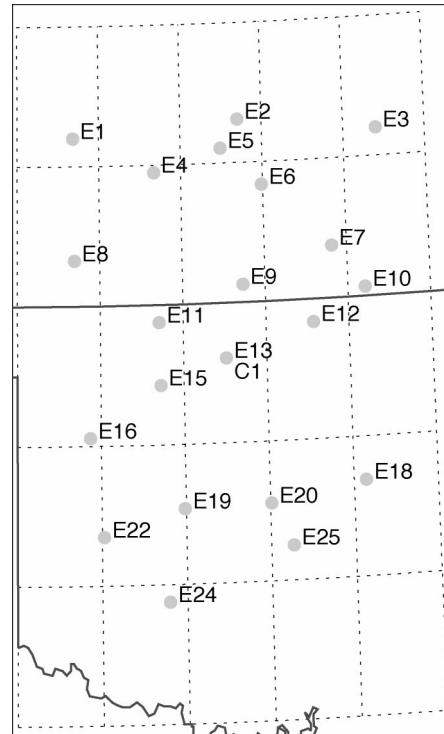

FIG. 1. Locations of extended facility MFRSRs at the DOE ARM program CART site in the SGP. The location of the E13 instrument coincides with the central facility C1.

size, and NO_2 and ozone column amounts. As part of the data processing, a spectrally self-consistent instrument calibration is determined from the data. In this paper we describe scaling properties of the aerosol optical thickness (AOT) at the 550-nm wavelength. This (derived) parameter has been selected as it facilitates direct comparison with other AOT measurements, in particular with the MODIS level-2 aerosol product. To ensure that the retrieval uncertainties have not affected the AOT scaling properties, the main computations of this study were repeated for the AOT at 870 nm, where aerosol is the sole contributor to the measured optical thickness. The results showed no systematic differences in scaling exponents between the two wavelengths (while the amplitude of AOT fluctuations at 870 nm is, of course, smaller, than at 550 nm).

The ARM MFRSR network at SGP consists of 21 instrument sites distributed throughout the area of approximately $3° \times 4°$ in north-central Oklahoma and south-central Kansas (Fig. 1). The principal dataset we use in this study consists of daily AOT time series derived from SGP MFRSR measurements made in the month of September 2000. Cloudless intervals suitable for the derivation of aerosol properties were selected through manual cloud screening. September 2000 was selected because of the large number of clear and partly clear days: most of the network instruments observed substantial clear-sky periods on at least 20 days during
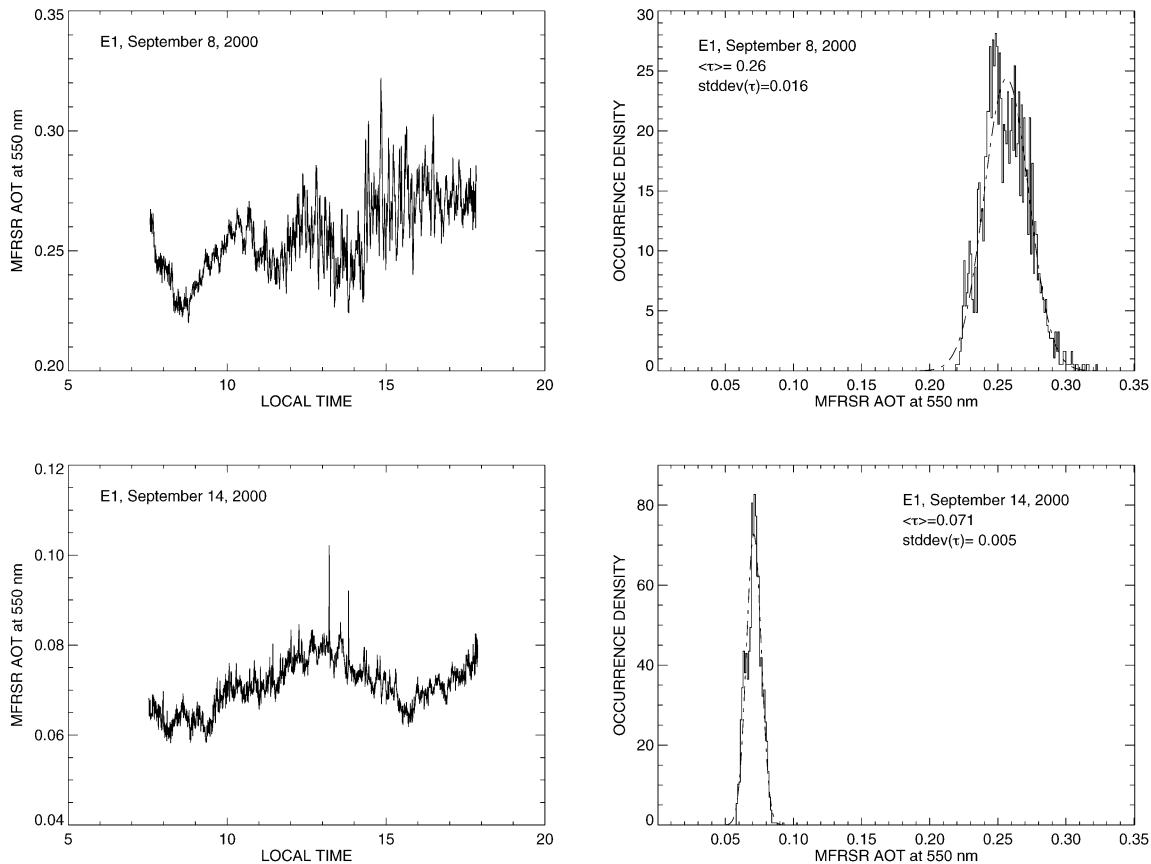
FIG. 2. (left) MFRSR-derived time series of AOT at 550-nm wavelength obtained on 8 and 14 Sep 2000 at SGP E1; (right) distribution densities of the values from the plots on the left, dashed–dotted curves show the Gaussian distributions with the same means and standard deviations.

this month. While aerosols at the SGP site come from a variety of local and remote sources (agricultural activities, pollution from industrial areas, fire smoke, and even Saharan dust), no significant pollution transport events were reported for September 2000. Thus, in this study we deal with the ambient aerosol properties. The density and homogeneity of this network allows us to construct 2D AOT maps for comparison with satellite data products (Alexandrov et al. 2002a). These features of the SGP network are also useful for scaling analysis providing for ensemble averaging in the case of AOT time series and allowing the spatial structure of AOT fields to be studied in the scale range of 30–400 km.

b. Data examples and traditional AOT statistics

Figure 2 (left panels) presents an example of MFRSR-derived AOT time series. The plots represent the measurements at the extended facility E1 made on 2 days (8 and 14 September) with high and moderate mean AOT, respectively. The traditional set of parameters describing the AOT variability, the mean, and the standard deviation are sufficient statistics to estimate the parameters of a Gaussian distribution. The use of these sta-

tistics implicitly assumes that the AOT variability on temporal scales up to 1 day is well approximated by a Gaussian distribution. The right panels of Fig. 2 confirm that this is a reasonable assumption if the data do not have a significant trend. Our measurements show a strong correlation between daily mean AOTs and the daily AOT standard deviations shown in Fig. 3. The values of AOT means and standard deviations presented there are averages over all available measurement sites for each day of September 2000. Records containing at least 500 data points were selected for averaging. The averaging might reduce the variability of individual site data resulting in an 86% correlation between the AOT means and standard deviations. On average the daily AOT standard deviation constitutes 13% of the mean. Long-term AOT statistics involving seasonal and interannual variations are well described in the literature based on both MFRSR data (Alexandrov et al. 2002c; Michalsky et al. 2001) and AERONET measurements (Holben et al. 2001). At such large temporal scales the positivity of AOT starts to manifest itself in the shape of statistical distribution functions making them lognormal rather than normal (O'Neill et al. 2000).
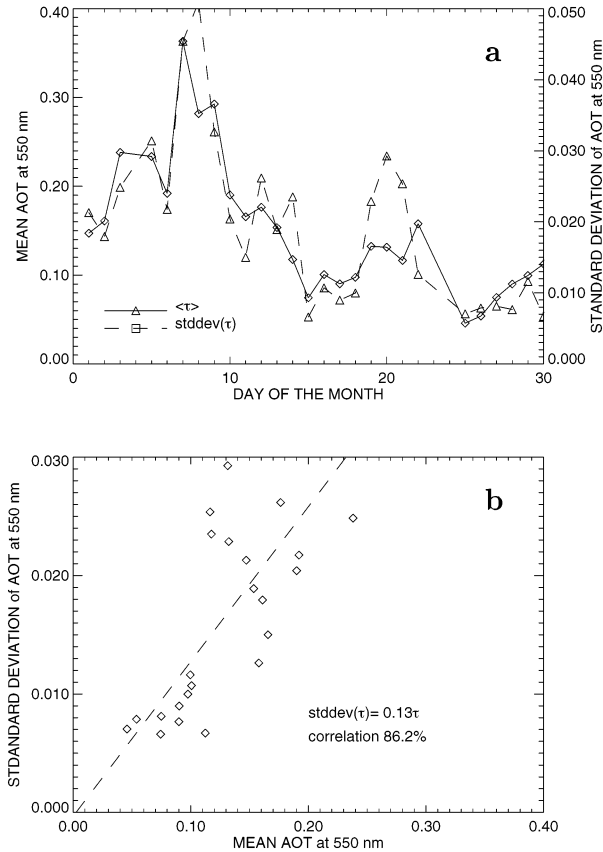
FIG. 3. (a) Time series of daily mean AOT and its standard deviation averaged over all measurement sites for Sep 2000; and (b) scatterplot showing strong correlation between time series in (a).

3. Scale analysis techniques

The mean and standard deviation are essentially one-point statistics; that is, the order of data values within a time interval is being ignored and replaced by a purely statistical set of parameters characteristic of the interval as a whole. Thus, the interval effectively collapses into a point with some average properties assigned to it. This approach leads to a scale truncation of the data variability; for example, the sequence of daily means and standard deviations does not contain information about hourly or minute variability. In this study we propose to add another parameter to the traditional two, which will relate AOT variabilities at different scales. It comes from the scale analysis approach that has become popular in recent years for studies of various geophysical phenomena (Turcotte 1997). For example, for clouds, scale-by-scale analysis provided a better understanding of cloud structure (Davis et al. 1999) and enabled the radiative smoothing scale to be identified (Marshak et al. 1995; Davis et al. 1997).

We start with a brief description of some basic scale analysis techniques, which will then be applied to AOT data.

a. Variance spectrum

Let $\varphi(x)$ be a realization of a real-valued stochastic process for $0 \leq x \leq L$ (x is time or a spatial variable). Then the variance (energy) spectrum $E(k)$ is defined as

$$E(k) = \frac{2}{L}|\hat{\varphi}(k)|^2, \qquad k > 0, \qquad (1)$$

where $\hat{\varphi}(k)$, $-\infty < k < \infty$ is the Fourier transform of $\varphi(x)$. Here, $E(k)$ is related to the variance of $\varphi(x)$:

$$\mathrm{var}(\varphi) = \overline{|\varphi(x) - \overline{\varphi}|^2} = \frac{1}{L}\int_0^L |\varphi(x) - \overline{\varphi}|^2\,dx$$

$$= \int_0^\infty E(k)\,dk, \qquad (2)$$

where the overbar denotes the average in x over L. Scale invariance of the field $\varphi(x)$ implies a power-law dependence of $E(k)$:

$$E(k) \propto k^{-\beta}, \qquad (3)$$

with $0 < \beta < 3$. Processes with $\beta \leq 1$ are stationary [i.e., $\varphi(x)$ is statistically invariant under translation in x]. If $1 < \beta < 3$, the field is nonstationary; however, it has stationary increments (Monin and Yaglom 1975; Davis et al. 1994). This means that $\varphi(x + r) - \varphi(x)$ is statistically independent of x, a fact used below in the definition of structure functions (note that for this property to be observed for a particular realization, r should be sufficiently small compared to L). As β approaches 3, the fluctuations diminish and the realizations start to look like smooth functions of x. The standard technique for determination of β is a linear fit to the plot of $\log[E(k)]$ versus $\log(k)$. The theoretical values of the β characteristic for wind speed and the passive scalar advection in turbulent processes are 5/3 for Kolmogorov's (1941) 3D turbulence, 3 for 2D turbulence (e.g., Gage and Nastrom 1986), and 1 for 3D turbulence near the surface (e.g., Nikora 1999). In our study we encounter the values of β ranging between 1.2 and 2.2 over a wide range of scales. Examples of simulated AOT scale-invariant time series for $\beta = 1.2$, 1.67, and 2.0 are shown in Fig. 4. The values of β are the only differences between these examples: the mean value, the standard deviation (8% of the mean), and the set of (random) phases of the Fourier components are the same in all three cases. In practice the spectra $E(k)$ may be quite noisy, and averaging of the regression plots $\log[E(k)]$ versus $\log(k)$ over an ensemble of realizations is needed to reveal the scale invariance of a dataset.

b. Structure functions

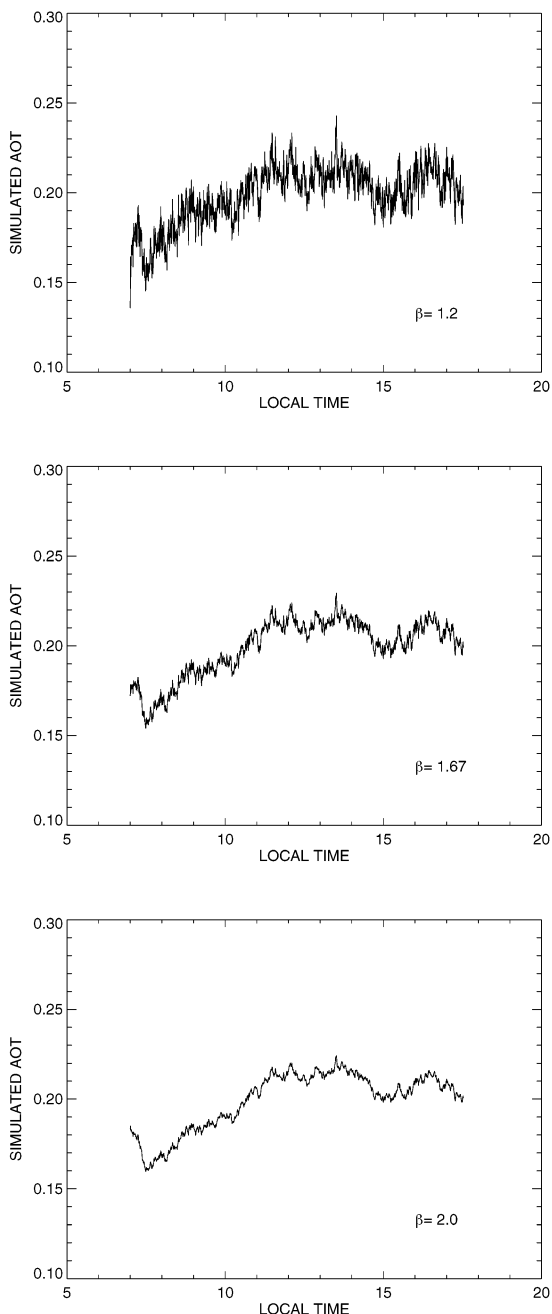A structure function of order $q > 0$ is defined in the 1D case as

FIG. 4. Simulated examples of scale-invariant AOT time series having the same mean and standard deviation (8% of the mean), but with different variance spectrum exponents $\beta = 1.2$, 1.67, and 2.0.

$$S_q(r) = \overline{|\varphi(x + r) - \varphi(x)|^q}$$

$$= \frac{1}{L - r} \int_0^{L-r} |\varphi(x + r) - \varphi(x)|^q \, dx. \quad (4)$$

Here the overbar stands for averaging in x, implying that an ergodicity hypothesis is valid and an ensemble average over realizations is equivalent to an average over x (time or space). Structure functions are defined in a similar manner for the 2D case:

$$S_q(r) = \overline{|\varphi(\mathbf{x} + \mathbf{r}) - \varphi(\mathbf{x})|^q}, \quad (5)$$

where $\mathbf{x}$ and $\mathbf{r}$ are now 2D vectors and $r = |\mathbf{r}|$. The form of the structure function (5) implicitly assumes statistical isotropy of the field $\varphi(\mathbf{x})$. Computation of structure functions is straightforward and (unlike with Fourier spectral methods) data gaps can be easily handled. Note that S_2 is often referred to as "the" structure function in turbulence literature, or as a variogram in geostatistics. For scale-invariant fields, S_q are power-law functions of r:

$$S_q(r) \propto r^{\zeta(q)}, \quad (6)$$

where $\zeta(q)$ is a monotonically nondecreasing concave function of q, $\zeta(q \to 0) \to 0$, if φ is bounded (Marshak et al. 1994). Using $\zeta(q)$, a nonincreasing hierarchy of exponents, H_q, is defined:

$$H_q = \frac{\zeta(q)}{q}. \quad (7)$$

If exponents H_q do not depend on q, the field φ is classified as monofractal (monoaffine, and is said to exhibit simple scaling) and is otherwise classified as multifractal (multiaffine, and exhibits anomalous scaling). Multifractality is caused by the presence of a range of singularities in the dataset, the stronger ones occurring intermittently. The small-scale intermittency of AOT datasets has been found to be negligible in our preliminary study (Alexandrov et al. 2003), and we do not therefore address this issue here. For one-dimensional fields $H_1 = 2 - D(\varphi)$, where $D(\varphi)$ is the fractal dimension of the graph $\varphi(x)$ in the plane. Here, $H_1 = 1$ corresponds to essentially 1D (almost everywhere) differentiable functions while $H_1 = 0$ (stationary case)—to graphs filling a 2D area. The Wiener–Khinchine relation (Monin and Yaglom 1975) applicable to nonstationary processes with stationary increments states that the second-order structure function S_2 is in Fourier duality with the energy spectrum $E(k)$ that results in the relation (e.g., Mandelbrot 1982)

$$\beta = \zeta(2) + 1 = 2H_2 + 1 \geq 1. \quad (8)$$

Note that in the case of simple scaling $H_2 = H_1 = H$ and $\beta = 2H + 1$. As in the case of variance spectra, ensemble averaging of structure functions can reduce noise and provide a better estimate of their typical behavior. Below we will not introduce special notations for ensemble-averaged structure functions, since it will be always clear from the context if the averaging has been applied.

4. Scaling properties of AOT time series: Variance spectra

In this section we apply the variance (energy) spectrum analysis described above to the SGP MFRSR net-
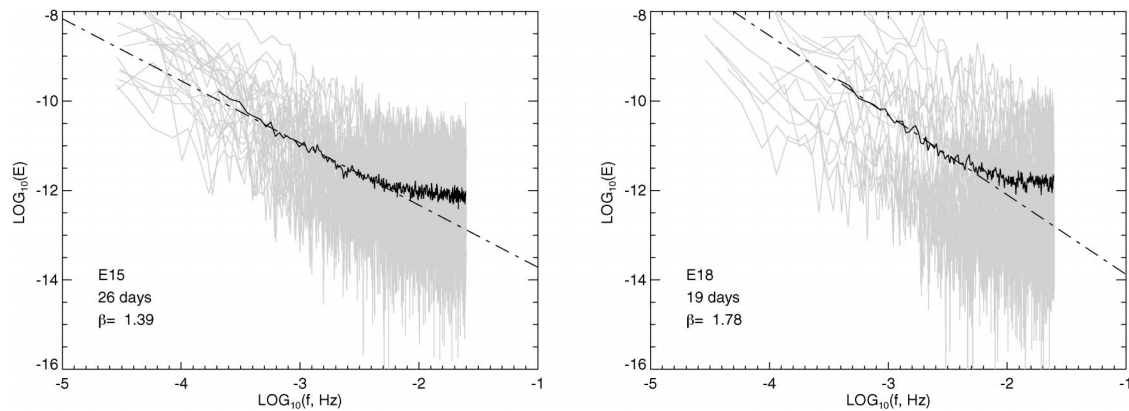
FIG. 5. Daily AOT variance spectra from two SGP extended facilities obtained from the Sep 2000 data (gray) and their time average (solid black curves); dotted–dashed lines represent the linear fits. The deviation from the linearity at frequencies higher than 0.01 Hz is caused by the instrument digitization noise.

work data, which we consider as an ensemble of individual (from single site and single day) AOT records. Removal of cloudy intervals from daily optical thickness datasets results in the presence of gaps in the data. These gaps do not affect structure function analysis; however, for Fourier analysis only gap-free intervals were selected. Gray curves in Figs. 5 and 6 represent individual AOT variance spectra. The noisiness of these spectra makes averaging over many sites and/or days necessary to reveal scale-invariant properties of the datasets. Figure 5 shows an example of time averaging for two MFRSR sites. The individual spectra plotted in gray on a logarithmic scale are averaged together to provide the monthly mean spectra shown by the black curves. These curves exhibit linearity (scale invariance) in a broad range of frequencies. The deviation from this linearity at frequencies higher than 0.01 Hz (corresponding to time intervals less than 1–2 min) is a consequence of the presence of digitization noise in the instrument data (MFRSR raw data are in discrete counts). A similar picture emerges when the spectra of data taken at a

number of sites on a given day are averaged, as is shown in Fig. 6.

Consistency requires that the average spectrum be the average of the same set of individual spectra at all frequencies. Therefore, the range of frequencies of the average spectrum is equal to the shortest range among the individual spectra. Thus, the minimal length of the individual gap-free interval allowed to be used in the averaging should be carefully determined: allowing it to be too short will result in a reduced frequency range, while requiring it to be too long results in a noisier spectrum. We chose a minimal daily interval length of 100 data points (2000 s ≈ 30 min) for averaging over sites or days.

Different types of averaging provide an insight into different properties of the dataset. Spatial averaging provides information on evolution of the spectral parameters in time, while averaging over time allows the spatial variability of AOT spectra to be studied. To explore AOT scaling at larger scales we apply averaging over both sites and days. This allows us to select enough
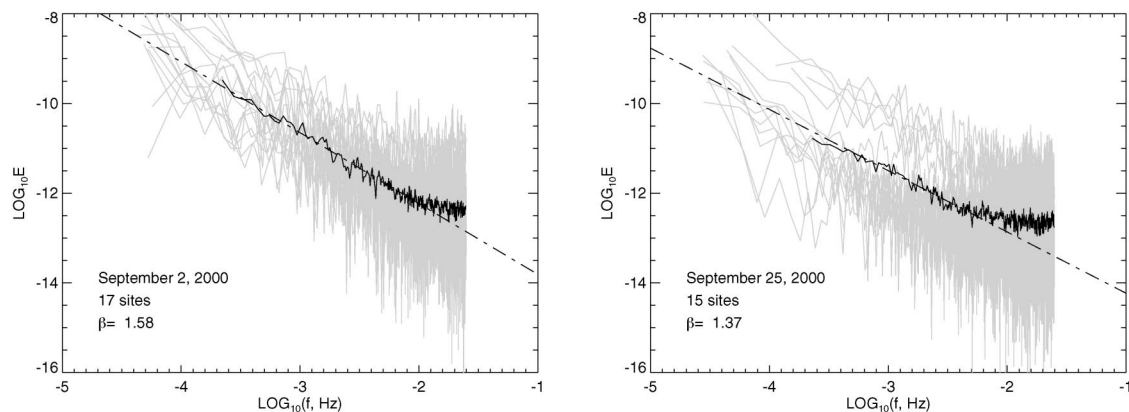

FIG. 6. AOT variance spectra obtained from available extended facilities data on 2 days in Sep 2000 (gray) and their spatial (ensemble) average (solid black curves); dotted–dashed lines represent the linear fits.
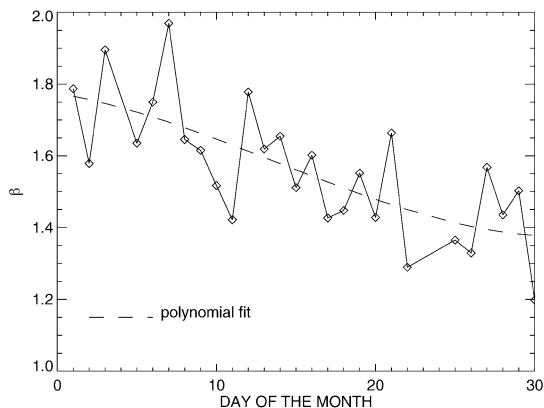
FIG. 7. Decrease of the (averaged over all sites) exponent β through the month of Sep 2000.
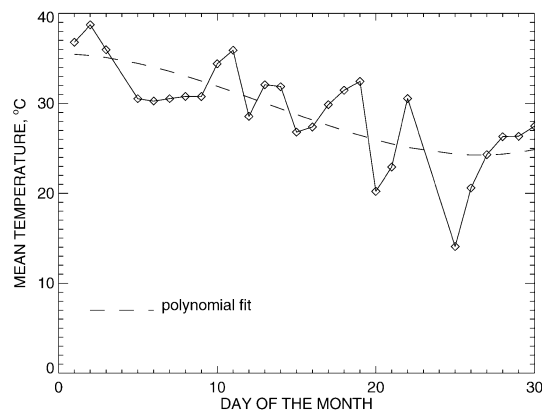

FIG. 8. Ground temperature record for Sep 2000.

records with sufficiently long clear intervals. We will describe some observed effects related to the structure of the atmospheric turbulence, such as the scale break, and the relationship of the spectral exponent β to the height of the aerosol layer and to the underlying topography. We, however, recognize that further extensive and complex data analysis is needed to identify, or constrain, a rigorous theory of these effects. Our suggested explanations represent a working hypothesis that we can use to guide that further analysis to either reject, or accept, the hypothesized reason for the observed AOT variability.

a. Temporal evolution of AOT variance spectra

Averaging the individual spectra over all MFRSR sites for a given day (Fig. 6) resulted in the time series of the daily values of β shown in Fig. 7. The decrease is clearly seen from $\beta \approx 1.8$ in the beginning of September 2000 to the values about 1.4 by the end of the month. We can find an explanation for this behavior by examining the change in meteorological conditions at the SGP site. As is seen from Figs. 8 and 9a, temperatures both at the surface and within the first 2–2.5 km of the atmosphere significantly decreased during the month (ground temperature dropped on average from 35°C to 20°–25°C). Figure 9 shows the corresponding changes in the mixed-layer structure. The mixed layer (also called the convective boundary layer) is the part of the atmosphere most directly affected by solar heating of the ground surface. In midlatitudes over land this layer typically reaches a height of 1–2 km by midafternoon (Kaimal et al. 1976). Its upper limit is often singled out by a capping inversion. As a result of strong convective vertical mixing, this layer exhibits a nearly constant distribution of potential temperature. Potential temperature is defined as

$$\Theta = (T + T_0)\left(\frac{P_0}{P}\right)^{\kappa} - T_0, \tag{9}$$

where T is atmospheric temperature (in °C), P is the pressure, $T_0 = 273.15$ (for °C to K conversion), $P_0 = 1013.25$ MB is the standard pressure, and $\kappa \approx 0.2854$ is the Poisson constant. The potential temperature profiles derived from radiosonde measurements taken during the afternoons throughout the month over the SGP Central Facility (CF; collocated with E13) are shown in Fig. 9a. The constant potential temperature segments and the corresponding capping inversions are well determined for most days presented except the very beginning of the month when the potential temperatures within the mixed layer were almost as high as those above it making the capping inversions hardly recognizable. The boundary of the mixed layer is associated with a sharp drop in relative humidity, for example, from 80% to 35% as is seen in data from 8 September (Fig. 9b). This suggests that the scattering tropospheric aerosol particles are confined mostly within the mixed layer. Small dry particles are present everywhere in the troposphere; however, they need humidification to play a role in the light scattering. This suggestion is confirmed by comparison of the aerosol scale height (Fig. 9c) and the mixed-layer height daily time series presented in Fig. 9d. Both parameters have similar values of 1.5–2.5 km and exhibit a similar decrease toward the end of the month. The mixed-layer height L_{MIX} is defined by the position of the capping inversions in Fig. 9a, and the aerosol scaling height L_{SC} was derived from daily daytime mean Raman lidar aerosol backscatter profiles by approximation of the portion of these profiles between 0.2 and 3.4 km by constant $\times \exp(-h/L_{SC})$. The Raman lidar is located at the SGP CF. The decrease in the mixed-layer height may also explain the decrease in total AOT (Fig. 3a). This requires an assumption that aerosol condensation centers are uniformly distributed over height and that their contribution to AOT depends only on the ambient relative humidity, that is, whether they are above or below the mixed-layer boundary. No correlation between ground relative humidity and AOT was observed.
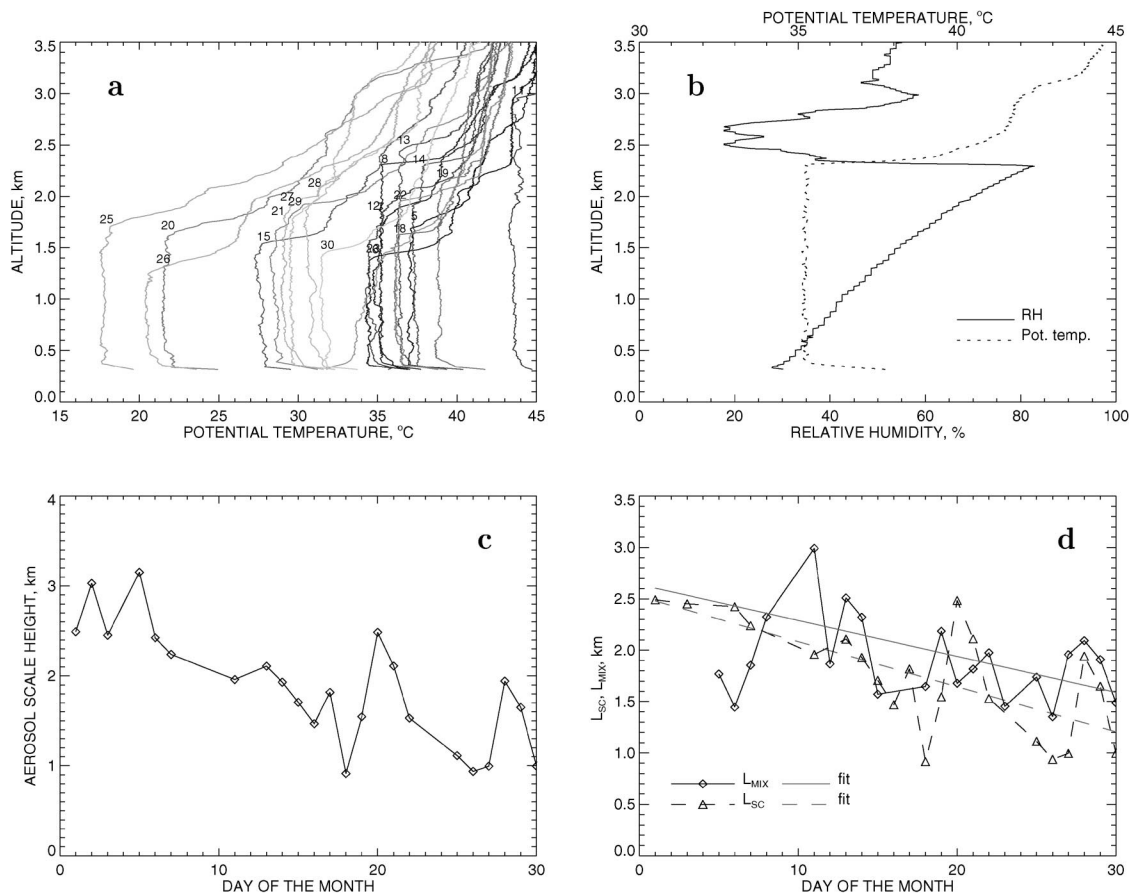
Fluctuations in AOT are governed by turbulent ex-

FIG. 9. (a) Potential temperature profiles derived from sonde data from midday flights during Sep 2000; darker curves correspond to earlier days of the month, and dates are printed near the mixed-layer boundaries. (b) An example of the relation between vertical profiles of relative humidity and potential temperature; both profiles are derived from sonde data from 8 Sep 2000. (c) Aerosol scale height time series derived from the CF Raman lidar profiles of the aerosol backscatter coefficient. (d) Mixed-layer height time series obtained from potential temperature profiles (a) in comparison with the aerosol scale heights (c); linear trends are shown in gray.

change in the mixed layer. In the present study we do not attempt to separate between the effects on AOT of direct variation in aerosol particle concentrations (El-perin et al. 2000) and of fluctuation in aerosol scattering properties caused by changes in particles size due to advection-related humidification (Schwartz 1998). In either case one expects the variance spectra of AOT to be similar to those of turbulence parameters, such as fluctuations of wind speed components and temperature. The latter spectra (Kaimal et al. 1976) exhibit Kolmo-gorov's scaling with $\beta = 5/3$ for high frequencies that decreases to values lower than 1 at low frequencies. Our observations are in the intermediate spectral range where the slope of the spectrum (in logarithmic scale) is roughly between 1 and 5/3. The value of $\beta = 1$ is associated with the maximum of the function $k E(k)$. The wind and temperature spectra of Kaimal et al. (1976) were obtained at a range of altitudes within the mixed layer. The position and magnitude of the maxi-mum in the spectra appears to depend on the altitude of the measurements: at higher altitude the maximum

has larger value and occurs at a lower frequency. This effectively increases the spectral slope β in the inter-mediate range with the altitude increase. Our results displayed in Fig. 10 support this argument. We observe a correlation of 58% between the aerosol scale height record (Fig. 9c) and the values of β (Fig. 7), which increases to 90% if data have a 3-day moving averaging applied to them (Figs. 10c,d). Correlations between β and total AOT and β and the surface temperature are weaker: both are about 70% after 3-day averaging.

b. Larger scales and the scale break

To study the AOT scaling in a wider spectral range we selected a set of individual records with a minimal length of 1500 data points = 30 000 s ≈ 8.5 h and performed averaging over both days and sites. The re-sulting spectrum is presented in Fig. 11. The difference in scaling between the high- and low-frequency spectral regions is evident: the value of the scaling exponent β = 1.48 at small scales is smaller than that of Kolmo-
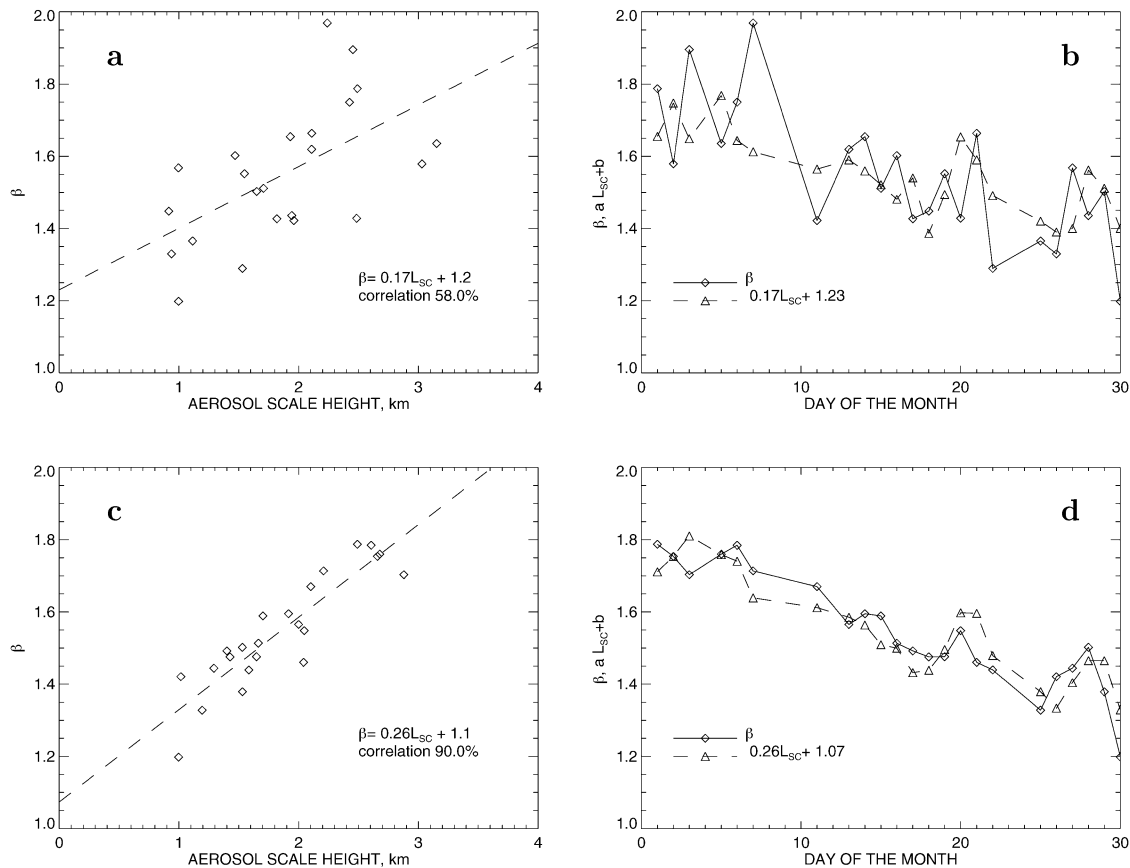
FIG. 10. Correlation between daily values of β and aerosol scaling heights (Fig. 9c): (a) scatterplot, (b) β time series (solid curve) in comparison with β record constructed from this for aerosol scaling heights using the linear relation from (a) (dashed curve); (c) and (d): the same as in (a) and (b) but for data smoothed over three subsequent days.

gorov's law ($5/3 \approx 1.67$), while the large-scale value of 1.95 exceeds the 5/3. The change in the slope of the variance spectrum plot (so-called scale break) occurs at the frequencies of $3–4 \times 10^{-4}$ Hz, corresponding to time scales of 2500–3000 s. Taking a typical wind speed of 5 m s^{-1} as a conversion factor, we obtain an estimate
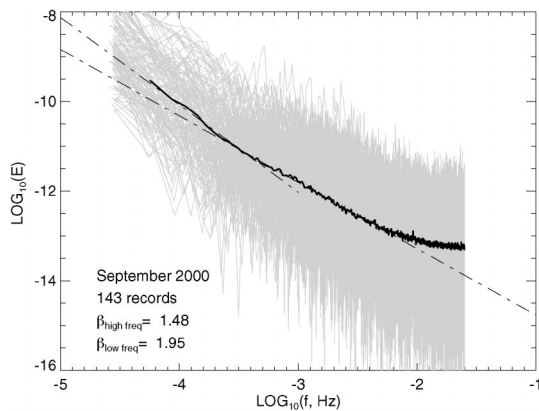

FIG. 11. Spectra averaged over all sites and all days with a continuous clear interval of at least 1500 data points (30 000 s = 8 h, 20 min); scale break is clearly seen.

of the scale break's spatial scale of 12–15 km. This behavior reflects the fact that most of the aerosols contributing to the observed AOT are confined within the mixed layer and are effectively separate from the upper troposphere. The mixed-layer height L_{MIX} is 1–3 km, and turbulent eddies of sizes smaller than this height are essentially 3D and therefore have spectral exponents close to the Kolmogorov's law for 3D turbulence ($\beta = 5/3$). Eddies larger than the mixed-layer height cannot fit into the mixed layer while maintaining 3D turbulent structure. The transition toward large-scale 2D turbulence (with $\beta = 3$) therefore starts with an increase of the eddy size beyond the scale of L_{MIX} (Lovejoy et al. 1993). This transition becomes detectable for scales substantially exceeding L_{MIX} (4–5 times in our case); however, within the available scale range β does not reach the value of 3 and remains essentially constant. Similar scaling behavior (3D to 2D transition) has been observed in a study of wind and temperature fluctuations in the free troposphere at 9–14-km altitude (Gage and Nastrom 1986). The scale ranges of these observations (up to 10 000 km) are much larger than in our dataset. The scale break was detected at around 500-km scale,

which, similarly to our case, significantly exceeds the characteristic thickness of the atmospheric layer studied.

c. The spectral exponents and the site topography

The geographical distribution of the monthly mean power spectrum exponent β (higher-frequency values only) is shown in Fig. 12. This distribution exhibits some correlation with the terrain properties, the surface curvature in particular. The altitude at the SGP site increases from about 200 m in the southeast to about 600 m in the northwest of the area. The major landscape inhomogeneity near the center of the site is related to the Cimarron River valley cutting through the altitude slope. This feature is well seen in the structure of the altitude-level curves plotted over the β map in the top-right panel of Fig. 12. These level curves represent a simplified model of the SGP terrain obtained by applying 2D spline interpolation to the set of MFRSR network sites altitudes. This operation is similar to a smoothing up to a 80-km scale (average distance between sites). Our model terrain is quite approximate. However, while being sufficiently accurate for our qualitative analysis, it is smooth, so its local curvature can be computed. As it can be seen from Fig. 12 (bottom panels), the structure of the level curves of this mean curvature resembles the spatial distribution of β. The mean curvature is a second-order-derivative characteristic of a surface, which in our case was calculated using the formula (Dubrovin et al. 1986)

$$K(x,\ y) = \operatorname{div}\!\left(\frac{\operatorname{grad}h}{\sqrt{1 + |\operatorname{grad}h|^2}}\right), \qquad (10)$$

or explicitly

$$K(x,\ y) = \frac{h_{xx} + h_{yy}}{(1 + h_x^2 + h_y^2)^{1/2}}$$
$$- \frac{h_x^2 h_{xx} + h_y^2 h_{yy} + 2h_x h_y h_{xy}}{(1 + h_x^2 + h_y^2)^{3/2}}, \qquad (11)$$

where $h = h(x,\ y)$ is the surface altitude as a function of geographical coordinates and the subscripts denote partial differentiation in longitudal and/or latitudal directions. The level curves of positive (concave surface) and negative (convex surface) values of the mean curvature are shown, respectively, in the bottom-left and -right panels of Fig. 12. The highest positive values are observed in the river valley and appear to correspond with higher values of β. On the other hand, the smallest negative curvature values at the valley banks correspond to minima in the β spatial distribution. We should note that this correspondence cannot be explained through a dependence on wind speed, because no pronounced differences were observed in the mean surface wind speed across the site. This correspondence may be a reflection of the known fact that the convex surface curvature suppresses turbulence intensities and concave curvature

causes an increase in boundary layer thickness and enhances turbulence intensities (Tulapukara et al. 2001). Cava et al. (2001) show a shift in the ground wind spectrum maximum toward lower frequencies over a complex (concave) terrain similar to the shift with measurement altitude noted above (Kaimal et al. 1976). Assuming that complex topography has a similar impact on turbulence spectra in our case, we can expect that under the same atmospheric conditions (temperature, mean wind speed, etc.) thicker layers and higher β will be observed over concave parts of the ground surface, compared to those observed over convex parts. The mechanism by which topography influences the mixed-layer properties is probably associated with the turbulence induced by the breaking of terrain-generated gravity waves (cf. Lilly and Kennedy 1973; Peltier and Clark 1983).

To ensure that the relation between β and the terrain properties is not accidental, we divided the MFRSR sites into two groups: the "high β" group with the monthly mean $\beta > 1.6$ and the "low β" group with $\beta < 1.6$. This division roughly coincides with the division by the sign of the mean surface curvature in Fig. 12 (bottom panels). Averaging individual daily spectra following the rules used for Fig. 11, but performing the ensemble averaging over the two groups separately, leads to the results shown in Fig. 13. It is seen that both the high- and low-frequency exponents for the high-β group are substantially larger than those for the low-β group (1.60 versus 1.35 and 2.08 versus 1.75). The separate averaging over the two groups was also applied to the construction of time series of daily (high frequency) β values similar to those in Fig. 7. The comparison shown in Fig. 14 allows us to observe the consistency in the difference between the exponent values for the two groups. The exponents in both groups decreased during the month showing coherence in day-to-day variability; however, βs from the "high" group were larger than those from the "low" group for almost every day. The only period when the differences were not pronounced was in the beginning of the month when both groups showed similarly high exponents. This may be a consequence of the weaker capping inversions during this period (see Fig. 9a), so that the geographical differences in the mixed-layer height have less effect on the turbulence structure and vertical distribution of aerosols. The identification of the spatial correlation between β and AOT or temperature is not conclusive because of the small variability of the latter two parameters across the SGP site.

5. Scaling properties of AOT time series: Structure functions

Averaging techniques similar to those described above for power spectra have also been applied to structure functions. Construction of the structure functions does not require continuity of the AOT time series, since
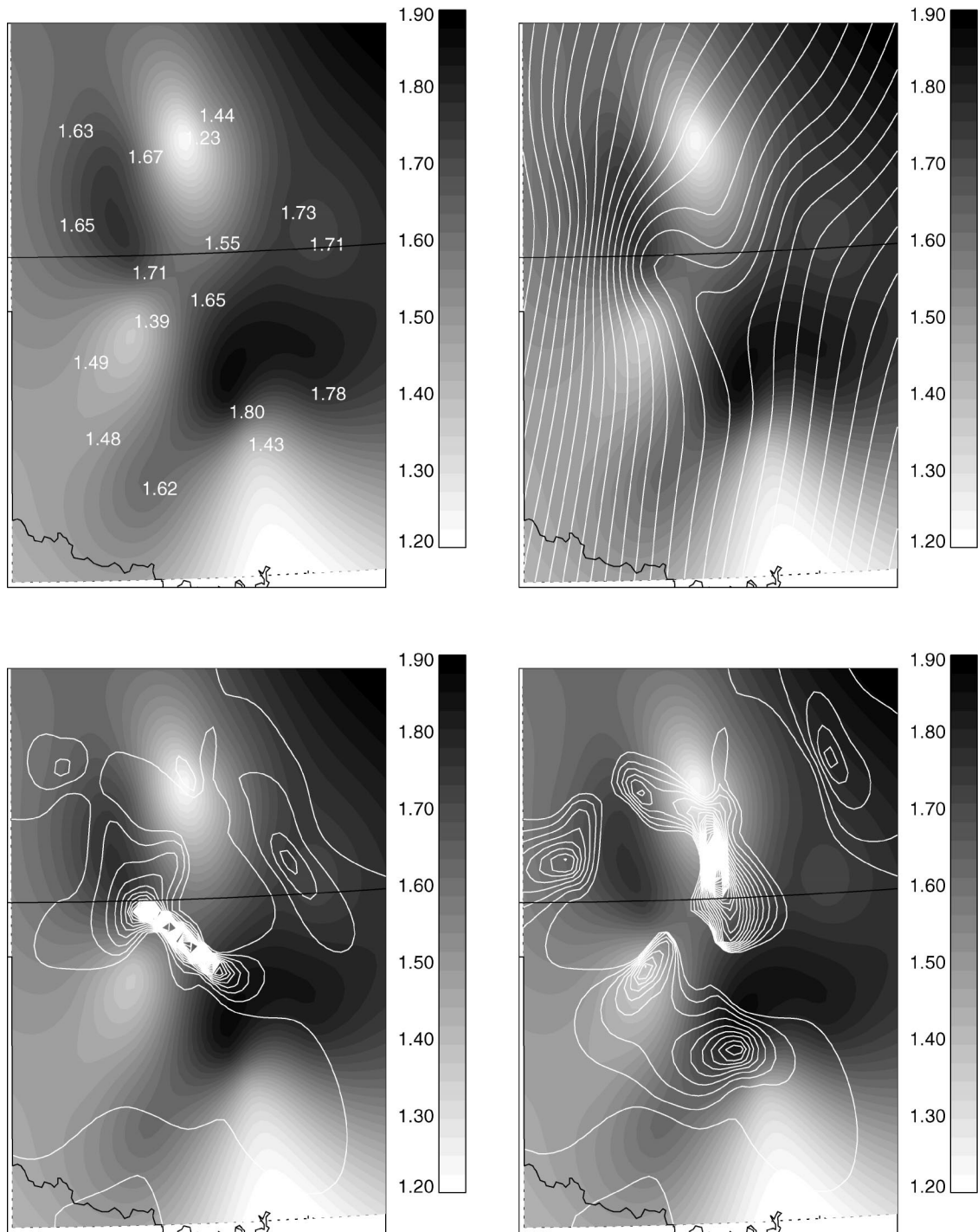
FIG. 12. (top left) The spatial distribution (spline surface with overprinted actual values) of the β exponent obtained from Sep 2000 monthly averaged energy spectra regressions; sites with at least 15 days of valid data (at least 100 data points in the longest gap-free segment) are taken. (top right) The same map with the overplotted level curves of the surface altitude (2D spline interpolation applied to the set of altitudes of MFRSR sites). (bottom) The same map but with overplotted level curves of the mean surface curvature, where it is positive (left) and negative (right).
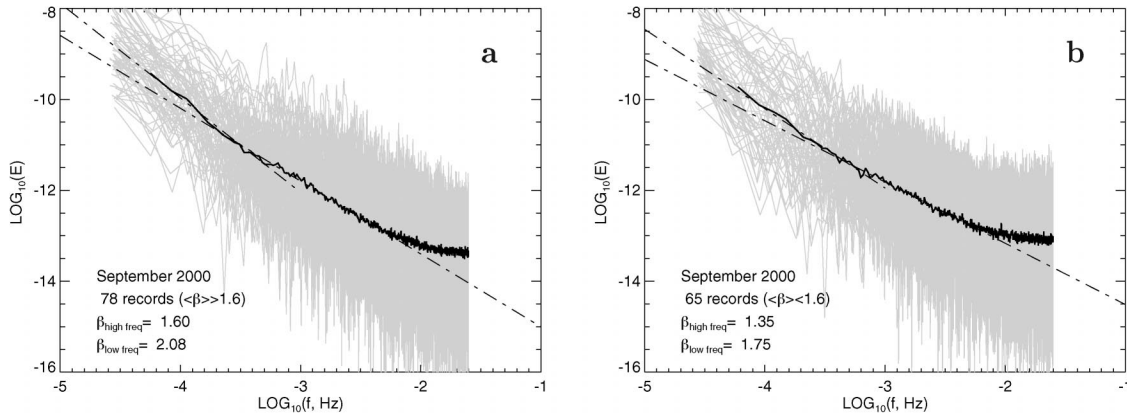
FIG. 13. Same as in Fig. 11 but with averaging separately over (a) high-β sites and (b) low-β sites.

the gaps in the data can be easily treated. Figures 15 and 16 present the second-order ($q = 2$) structure functions where the averaging is over time and space (ensemble), respectively. The minimum number of data points required for individual AOT datasets to be included into the averaging was 500. These figures are analogous to Figs. 5 and 6; however, the scale break corresponding to the transition from 3D to 2D turbulence with increasing scale is much more pronounced for structure functions than for power spectra and can be seen even in single-site or single-day plots (like Figs. 15a and 16b). The time series of daily structure function exponents (both high and low frequency) obtained by averaging over all MFRSR sites are shown in Fig. 17. For comparability with the results of the previous section we used the relation (8) and plotted the values of $2H_2 + 1$ instead of these of $H_2 = \zeta(2)/2$ itself. We see that the low-frequency exponent has almost no trend. The values of the high- and low-frequency exponents in the beginning of the month are close to each other, so the scale break is difficult to recognize in the daily structure function plots (cf., e.g., the 2 and 25 September plots in Figs. 16a and 16b). The structure functions of

the first and second orders averaged over all sites and all days with at least 1500 data points (30 000 s = 8 h, 20 min of time possibly with gaps) are shown in Figs. 18a and 18b, respectively. Note that our assumption of simple scaling ($H_1 \approx H_2$) is much better for small scales (high frequencies). The scale break is particularly well determined when averaging is performed over a large number (almost 200) of individual records.

The values of β obtained by the power spectra analysis (Fig. 7a) and the (high frequency) structure function exponents from Fig. 17 exhibit the same trend during the month and are well correlated (73%). However, the structure function exponents are systematically (by 0.13 on average) smaller than their power spectrum analogs, especially for the first half of the month. This difference, which contradicts relation (8), is caused by the fact that the dataset analyzed here is not strictly scale invariant (i.e., it has scale breaks). The spatial distribution of both high-frequency monthly mean structure function exponents is similar to that of the power spectrum exponent β (Fig. 12); therefore, we have not included a figure showing this distribution. The low-frequency exponents show lower correlation with the terrain properties (similar to the lower correlation with the L_{SC}, as can be seen from Fig. 17).
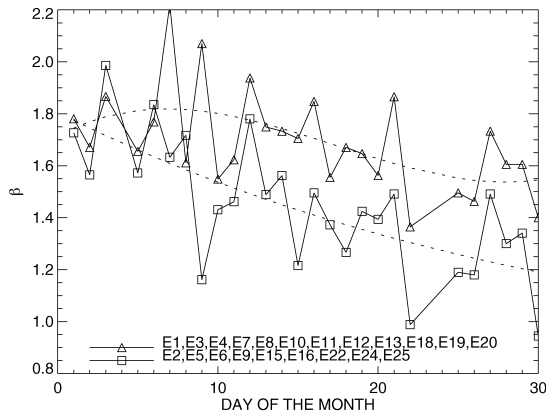
6. Spatial scaling of AOT

The density of MFRSR sites at SGP appears to be sufficient to determine AOT spatial scaling at ranges of up to 400 km. Figure 19a shows the first-order spatial structure function for 14 September 2000. Nineteen MFRSRs were operating on this day (all except E3 and E6). The measured optical thickness was moderate, and few clouds were present in the area.

The spatial structure functions for the MFRSR network data are defined similarly as in (5):

$$S_q(r) = \langle \overline{|\tau(\mathbf{x} + \mathbf{r}, t) - \tau(\mathbf{x}, t)|^q} \rangle, \qquad (12)$$

where $\mathbf{x}$ represents 2D vectors corresponding to sites' coordinates and $r = |\mathbf{r}|$ are distances between sites.

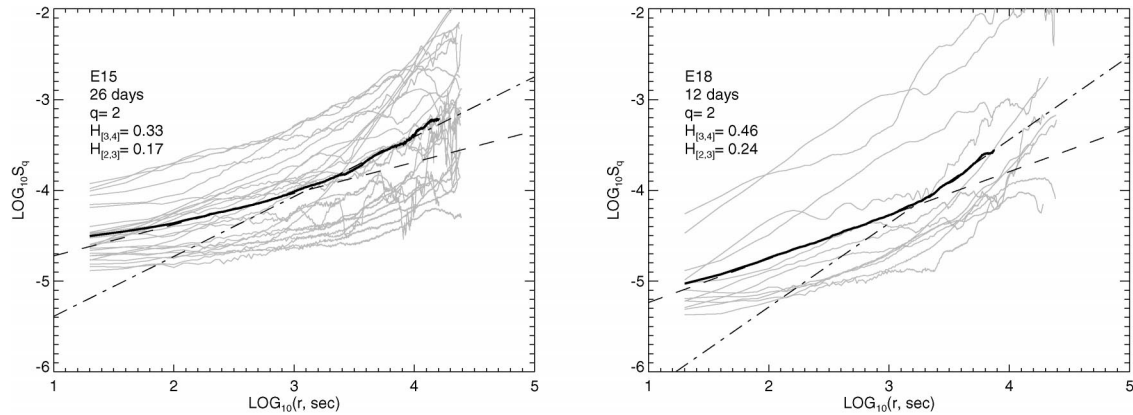FIG. 14. Same as in Fig. 7 but for the high- and low-β sites separately.

FIG. 15. Same as in Fig. 5 but for the second-order structure functions; only daily records with at least 500 data points were selected for averaging. The scale break is seen better in structure functions than in variance spectra. Here $H_{[2,3]}$ denotes the small-scale exponent (for $10^2 < r < 10^3$ s), and $H_{[3,4]}$ stands for the large-scale exponent (for $10^3 < r < 10^4$ s). In both cases $H = H_2 = \zeta(2)/2$, as in Eq. (7).

The overbar denotes temporal averaging, while the angle brackets denote spatial averaging in **x**. Practically, in order to obtain spatial structure functions (of the first order) we considered all 171 possible pairs of available sites. It appears that the set of distances between the sites in all these pairs provides a uniform coverage of the lag range from 30 to 415 km with an average spacing of 2.3 km. For each pair of sites (say, site 1 and site 2, located r_{12} km apart) time series of simultaneous absolute differences in AOT $|\Delta\tau(t)|_{12} = |\tau_1(t) - \tau_2(t)|$ were calculated. Then the temporal averaging over the day was applied and the quantities $|\Delta\tau|_{12} = \overline{|\Delta\tau(t)|}_{12}$ were computed. In Fig. 19a the data from individual pairs of sites (say, i and j running over the site numbers) are depicted by dots with horizontal coordinates equal to distances between the sites r_{ij}, and vertical coordinates equal to

$$|\Delta\tau|_{ij} = \overline{|\tau_i(t) - \tau_j(t)|}. \tag{13}$$

The subsequent averaging of $|\Delta\tau|_{ij}$ within 20-km bins (taking into account the number of data points used for each pair) reveals the statistical dependence on the distance between sites (space lag) r of

$$S_1(r) = \langle|\Delta\tau|_{ij}\rangle_{r_{ij}=r}. \tag{14}$$

This dependence is shown in Fig. 19a by the histogram-like solid line. This dependence can be closely approximated by a power-law function (dotted–dashed curve in Fig. 19a) with the power exponent H. It is seen from Fig. 19a that on that day AOT was likely to change by about 0.03 within 100 km, and by about 0.06 within 400 km. In general, as it follows from (6) the relation between variability in scales r_1 and r_2 is

$$S_1(r_1) = \left(\frac{r_1}{r_2}\right)^H S_1(r_2). \tag{15}$$

Unfortunately, the quality of the daily spatial structure functions for many days of the month is not as good as for 14 September 2000. Thus, the above-described regression averaging is necessary. The result of such averaging over the 29 clear days in September 2000 is shown in Fig. 19b with the resulting $H = 0.32$. The value of $H = 0.55$ for 14 September 2000 is larger than the average indicating stronger than average correlation in the AOT field on this day.

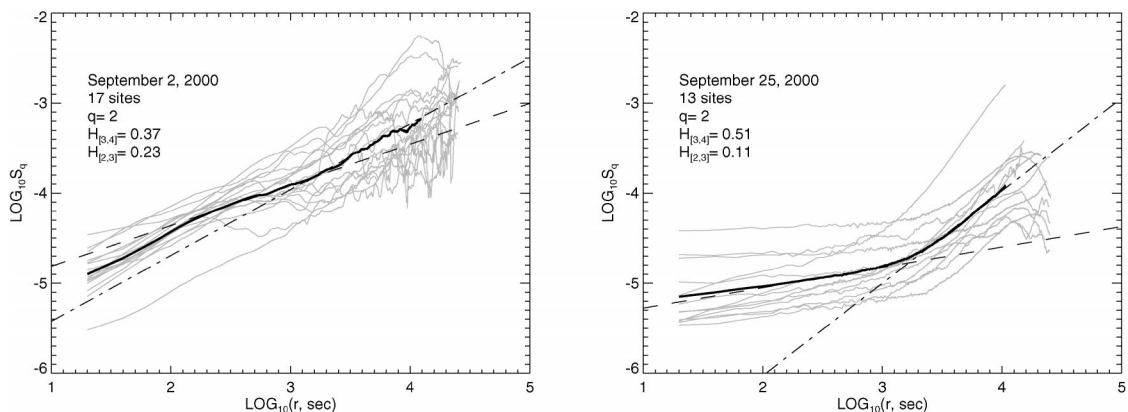The MFRSR network at SGP provides a unique op-

FIG. 16. Same as in Fig. 6 but for the second-order structure functions; see Fig. 15 for notation.
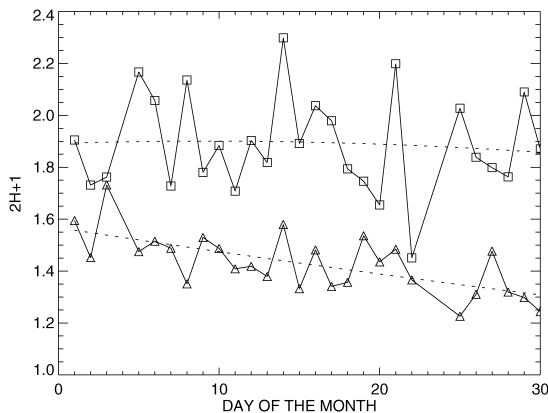
FIG. 17. Variations of high-frequency (bottom curve) and low-frequency (top curve) exponents $\beta = 2H_2 + 1$ of the AOT second-order structure functions during September 2000.

portunity to study space-to-time conversion. Because of the density of the network it is possible to evaluate the spatial correlations and to compare them with the temporal correlation to determine the validity range of Taylor's frozen turbulence hypothesis (Taylor 1915). This hypothesis states that the spatial variations (along the wind direction) of a turbulence field advected past a fixed point are due entirely to the mean flow. This implies that it can be derived from the time series measured at this fixed point using the mean wind speed to convert time into distance. Testing Taylor's hypothesis is important for determination of information content of turbulence-related experimental techniques based on one-point measurements. Comparing large-scale parts of the temporal structure functions plotted in Fig. 18a with their spatial counterparts from Fig. 19b, we can conclude that both spatial and temporal aerosol fluctuations after sufficient averaging follow the power law. However the cumulative scaling exponent for spatial fluctuations is lower than its temporal counterpart. Spatial and temporal structure functions also have different prefactors (imaginary intercepts of the straight line indi-

cating scaling and the vertical axis on log–log plots). While these results question the validity of Taylor's hypothesis at sufficiently large scales, more cases should be investigated before any firm conclusions are drawn.

It is worthwhile to notice that from the point of view of spatial correlation statistics, the dense MFRSR network data are a ground-based prototype of high-resolution satellite images (like MODIS aerosol retrievals). The correlation between pixels separated by a certain distance r in MODIS images can be studied in the same way as is described above for spatial statistics of the MFRSR network data. The structure function technique is particularly useful when the satellite retrievals have a sparse distribution of the retrieved AOT values due to clouds and high surface albedo in some pixels. Our results in this area will be reported elsewhere.

7. Summary and future research

In order to characterize the correlation between measurements of aerosol optical thickness (AOT) at different scales, the paper analyzes the AOT data collected in September 2000 from the dense local MFRSR network located in the southern Great Plains. Two simple complementary statistics, variance spectra and structure functions, were used for the analysis of spatial and temporal correlation in AOT. The scale-by-scale analysis indicates that temporal variability of AOT follows two stable scale-invariant regimes for small (0.5–15 km) and large (15–100 km) scales. Small-scale fluctuations are governed by 3D turbulence and are characterized by the spectral exponent $\beta \approx 5/3$ and the first-order structure function exponent $H \approx 0.3$. Large-scale fluctuations have higher $\beta \approx 2$ and $H \approx 0.4$–0.5. We suggest that this scaling regime corresponds to a transition toward large-scale 2D turbulence.

We found that the spectral exponent that characterizes small-scale fluctuations of AOT is in good correlation temporally with the aerosol scale height and spatially with the concavity/convexity of the site topography. A
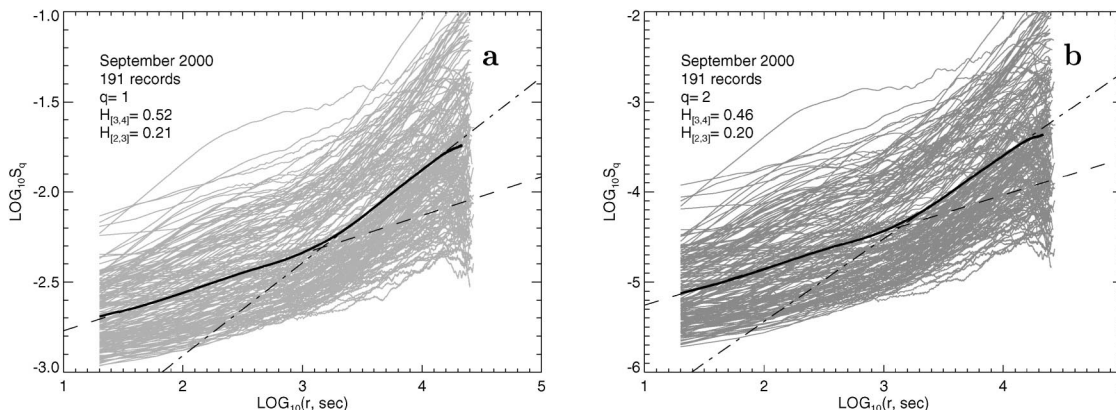

FIG. 18. Structure functions of the (a) first and (b) second orders averaged over all sites and all days with at least 1500 data points (30 000 s = 8 h, 20 min of time possibly with gaps); scale break is clearly seen. (See Fig. 15 for notation.)
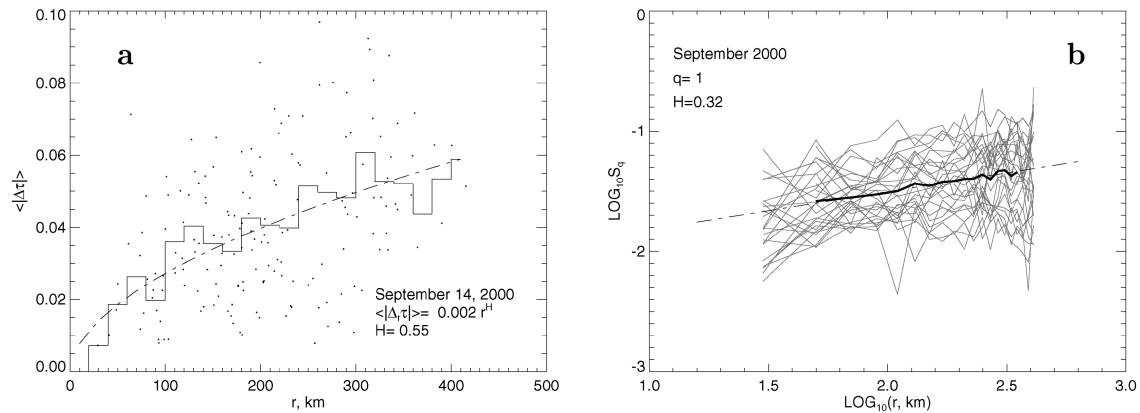
Fig. 19. Spatial scaling analysis of the AOT field measured by the SGP MFRSR network: (a) the first-order structure function $S_1(r) = \langle |\Delta_r \tau| \rangle$ for MFRSR network data obtained on 14 Sep 2000; the data from individual pairs of sites are depicted by dots, the solid line is the histogram of 20-km bin means, and the dotted–dashed curve is the power-law fit to this histogram. (b) Spatial first-order structure functions from all available sites averaged over 29 clear days in Sep 2000. Individual daily structure functions are plotted in gray.

rigorous theory for these correlations is still lacking, but we suggest turbulent mixing as a preliminary hypothesis. The large-scale fluctuations do not show much sensitivity to both the aerosol scale height and the site topography.

For the first time, Taylor's frozen-turbulence hypothesis used to convert space to time could be tested using the AOT data. Preliminary results show a scale-invariant behavior for both spatial (30–400 km) and temporal (15–100 km) fluctuations with values of spatial H smaller than the temporal ones and different prefactors. The analysis of spatial fluctuations in the AOT fields serves as a bridge to the analysis of aerosol variability retrieved from high-resolution satellite data. The results of comparisons between the two-point AOT statistics derived from MFRSR observations and those obtained from the MODIS level-2 aerosol product will be reported elsewhere. Note that in addition to having a large overlap range suitable for intercomparison (10–400 km), the ranges of the MODIS and MFRSR AOT datasets also complement each other: the ground-based measurements allow the microscale variability of AOT to be studied, while the satellite observations reveal the synoptic-scale behavior.

Our future plans in this area of research include the study of long-term datasets in order to determine the annual and interannual two-point statistical properties of AOT. We also plan to more fully investigate Taylor's frozen-turbulence hypothesis and to expand our focus to include other retrieval products such as aerosol particle size. We expect this kind of study to shed more light on the nature of aerosol variability. In particular, the scale dependence of correlations between particle size and AOT may help to separate the influence on AOT fluctuations of turbulence-driven aerosol concentration variations from that of variability in aerosol scattering properties due to humidification caused by convective advection.

REFERENCES

Alexandrov, M., A. Lacis, B. Carlson, and B. Cairns, 2002a: Derivation of 2D fields of aerosol and trace gases parameters by integrated analysis of multi-instrument MFRSR dataset from DOE ARM program CART site. *Proc. SPIE,* **4539,** 277–288.

——, ——, ——, and ——, 2002b: Remote sensing of atmospheric aerosols and trace gases by means of Multi-Filter Rotating Shadowband Radiometer. Part I: Retrieval algorithm. *J. Atmos. Sci.,* **59,** 524–543.

——, ——, ——, and ——, 2002c: Remote sensing of atmospheric aerosols and trace gases by means of Multi-Filter Rotating Shadowband Radiometer. Part II: Climatological applications. *J. Atmos. Sci.,* **59,** 544–566.

——, ——, ——, and ——, 2003: Atmospheric aerosol and trace gases parameters derived from local MFRSR network: Multi-instrument data fusion in comparison with satellite retrievals. *Proc. SPIE,* **4882,** 498–509.

Cahalan, R. F., and J. B. Snider, 1989: Marine stratocumulus structure during FIRE. *Remote Sens. Environ.,* **28,** 95–107.

Cava, D., U. Giostra, and M. Tagliazucca, 2001: Spectral maxima in a perturbed stable boundary layer. *Bound.-Layer Meteor.,* **100,** 421–437.

Davis, A., A. Marshak, W. Wiscombe, and R. Cahalan, 1994: Multifractal characterizations of nonstationarity and intermittency in

geophysical fields: Observed, retrieved, or simulated. *J. Geophys. Res.,* **99,** 8055–8072.

——, ——, ——, and ——, 1996: Scale invariance of liquid water distributions in marine stratocumulus. Part I: Spectral properties and stationarity issues. *J. Atmos. Sci.,* **53,** 1538–1558.

——, ——, R. Cahalan, and W. Wiscombe, 1997: The Landsat scale break in stratocumulus as a three-dimensional radiative transfer effect: Implications for cloud remote sensing. *J. Atmos. Sci.,* **54,** 241–260.

——, ——, H. Gerber, and W. Wiscombe, 1999: Horizontal structure of marine boundary-layer clouds from cm- to km-scales. *J. Geophys. Res.,* **104,** 6123–6144.

Dubrovin, B. A., A. T. Fomenko, and S. P. Novikov, 1986: *Modern Geometry—Methods and Applications.* Springer-Verlag, 759 pp.

Elperin, T., N. Kleeorin, and I. Rogachevskii, 2000: Mechanisms of formation of aerosol and gaseous inhomogeneities in the turbulent atmosphere. *Atmos. Res.,* **53,** 117–129.

Gage, K. S., and G. D. Nastrom, 1986: Theoretical interpretation of atmospheric wavenumber spectra of wind and temperature observed by commercial aircraft during GASP. *J. Atmos. Sci.,* **43,** 729–740.

Hansen, J., and Coauthors, 2002: Climate forcings in Goddard Institute for Space Studies SI2000 simulations. *J. Geophys. Res.,* **107,** 4347, doi:10.1029/2001JD001143.

Harrison, L., J. Michalsky, and J. Berndt, 1994: Automated multifilter shadow-band radiometer: Instrument for optical depth and radiation measurement. *Appl. Opt.,* **33,** 5118–5125.

Holben, B. N., and Coauthors, 2001: An emerging ground-based aerosol climatology: Aerosol optical depth from AERONET. *J. Geophys. Res.,* **106,** 12 067–12 097.

Houghton, J. T., Y. Ding, D. J. Griggs, M. Noguer, P. J. van der Linden, and D. Xiaosu, Eds., 2001: *Climate Change 2001: The Scientific Basis—Contribution of Working Group I to the Third Assessment Report of the Intergovernmental Panel on Climate Change.* Cambridge University Press, 944 pp.

Ivanova, K., E. E. Clothiaux, H. N. Shirer, T. P. Ackerman, J. C. Liljegren, and M. Ausloos, 2002: Evaluating the quality of ground-based microwave radiometer measurements and retrievals using detrended fluctuation and spectral analysis methods. *J. Appl. Meteor.,* **41,** 56–68.

Kaimal, J. C., J. C. Wyngaard, D. A. Haugen, O. R. Cote, Y. Izumi, S. J. Caughey, and C. J. Readings, 1976: Turbulence structure in the convective boundary layer. *J. Atmos. Sci.,* **33,** 2152–2169.

Kaufman, Y. J., D. Tanre, L. A. Remer, E. F. Vermonte, A. Chu, and B. N. Holben, 1997: Operational remote sensing of tropospheric aerosol over land from EOS moderate resolution imaging spectroradiometer. *J. Geophys. Res.,* **102,** 17 051–17 067.

——, ——, and O. Boucher, 2002: A satellite view of aerosols in the climate system. *Nature,* **419,** 215–223.

Kolmogorov, A. N., 1941: Local structure of turbulence in an incompressible liquid for very large Reynolds numbers. *Dokl. Akad. Nauk SSSR,* **30,** 299–303.

Lilly, D. K., and P. J. Kennedy, 1973: Observations of a stationary mountain wave and its associated momentum flux and energy dissipation. *J. Atmos. Sci.,* **30,** 1135–1152.

Lovejoy, S., D. Schertzer, P. Silas, Y. Tessier, and D. Lavalee, 1993: The unified scaling model of atmospheric dynamics and systematic analysis of scale invariance in cloud radiances. *Ann. Geophys.,* **11,** 119–127.

Mandelbrot, B. B., 1982: *The Fractal Geometry of Nature.* W. H. Freeman, 460 pp.

Marshak, A., A. Davis, R. Cahalan, and W. Wiscombe, 1994: Bounded cascade models as nonstationary multifractals. *Phys. Rev. E,* **49,** 55–69.

——, ——, W. Wiscombe, and R. Cahalan, 1995: Radiative smoothing in fractal clouds. *J. Geophys. Res.,* **100,** 26 247–26 261.

——, ——, ——, and ——, 1997: Scale invariance of liquid water distributions in marine stratocumulus. Part II: Multifractal properties and intermittency issues. *J. Atmos. Sci.,* **54,** 1423–1444.

Michalsky, J. J., F. A. Schlemmer, W. E. Berkheiser, J. L. Berndt, L. C. Harrison, N. S. Laulainen, N. R. Larson, and J. C. Barnard, 2001: Multiyear measurements of aerosol optical depth in the Atmospheric Radiation Measurement and Quantitative Links programs. *J. Geophys. Res.,* **106,** 12 099–12 107.

Monin, A. S., and A. M. Yaglom, 1975: *Statistical Fluid Mechanics: Mechanics of Turbulence.* Vol. 2. MIT Press, 874 pp.

Nikora, V., 1999: Origin of the "−1" spectral law in wall-bounded turbulence. *Phys. Rev. Lett.,* **83,** 734–736.

O'Neill, N. T., A. Ignatov, B. N. Holben, and T. F. Eck, 2000: The lognormal distribution as a reference for reporting aerosol optical depth statistics: Empirical tests using multi-year, multi-site AERONET sunphotometer data. *Geophys. Res. Lett.,* **27,** 3333–3336.

Peltier, W. R., and T. L. Clark, 1983: Nonlinear mountain waves in two and three spatial dimensions. *Quart. J. Roy. Meteor. Soc.,* **109,** 527–548.

Schwartz, S. E., 1998: Correlated short term fluctuations in aerosol optical thickness and shortwave radiative quantities. *Proc. Eighth Annual Atmospheric Radiation Measurement (ARM) Program Science Team Meeting,* Tucson, AZ, DOE, 657–660.

Taylor, G. I., 1915: Eddy motion in the atmosphere. *Philos. Trans. Roy. Soc.,* **A215,** 1–26.

Tulapukara, E. G., A. B. Khoshnevis, and J. L. Narasimhan, 2001: Wake–boundary layer interaction subject to convex and concave curvatures and adverse pressure gradient. *Exp. Fluids,* **31,** 697–707.

Turcotte, D. L., 1997: *Fractals and Chaos in Geology and Geophysics.* Cambridge University Press, 300 pp.